Chapter 5

HIGH-RATE MULTIPLEXED ENTANGLEMENT SOURCE BASED ON TIME-BIN QUBITS FOR ADVANCED QUANTUM NETWORKS

This chapter includes the work published as:

[1] Andrew Mueller, Samantha I. Davis, Boris Korzh, Raju Valivarthi, Andrew D. Beyer, Rahaf Youssef, Neil Sinclair, Cristián Peña, Matthew D Shaw, and Maria Spiropulu. "High-rate multiplexed entanglement source based on time-bin qubits for advanced quantum networks." In: Optica Quantum 2.2 (2024), pp. 64–71.

5.1 Introduction

Quantum computing represents an upcoming threat to public-key cryptography [1, 2]. Quantum Key Distribution (QKD) is a method for overcoming this threat by sharing secret cryptographic keys between parties in a manner that is sufficiently secure against potential eavesdroppers and the decryption capabilities of quantum computers. Point-to-point QKD networks are a precursor to more advanced quantum networks which enable the transfer of quantum states for multiple applications including distributed quantum computing, sensing, or secure communication. We characterize any quantum network as 'advanced' if it enables protocols and capabilities that go beyond point-to-point QKD [3]. These include teleportation [4, 5], entanglement swapping [6], memory-assisted networks [7], and others. Entangled photons are a fundamental resource for such demonstrations, and entanglement distribution is therefore a key component of premier quantum network initiatives including the European Quantum Communication Infrastructure (EuroQCI) project, the Illinois Express Quantum Network (IEQNET), the Chinese Quantum Experiments at Space Scale (QUESS) initiative, the United Kingdom UKQNTel network, and the Washington DC-QNet Research Consortium. Future quantum networks should enable high-fidelity and high-rate transfer of individual quantum states across multiple quantum nodes, mediated by distribution of entangled photons, quantum memories, and entanglement swapping measurements.

High-rate entanglement distribution enables high-rate entanglement-based QKD, as well as more general operations that characterize advanced quantum networks.

Entanglement distribution and entanglement-based QKD have been demonstrated with impressive performance across a number of metrics. These include 40 kbps data rates in a QKD system deployed over 50 km of fiber [8] as well as multiple polarization entangled sources that leverage spectral multiplexing. These polarization sources include a demonstration of 181 kebits/s across 150 ITU channel pairs and a high-throughput source potentially capable of gigabit rates with many added channels and detectors [9, 10]. Multiple works have highlighted the need to leverage high total brightness, spectral brightness, collection efficiency, and visibility from pair-generating non-linear crystals to realize practical high-rate entanglement distribution [10, 11, 12, 13, 14, 15, 16].

A time-bin entangled photon source has certain advantages over a polarization-based system [17]. Time-bin entanglement can be measured with no moving hardware and does not require precise polarization tracking to maximize visibility [18, 19]. Also, with suitable equipment, robust time-bin modulation is possible over free space links with turbulence [20]. Therefore, the possibility of simplified fiber-to-free-space interconnects and larger quantum networks based on a shared time-bin protocol motivates development of improved time-bin sources. Furthermore, time-bin encoding is suited for single-polarization light-matter interfaces [21].

We direct 4.09 GHz mode locked laser light into a nonlinear crystal via 80-ps delay-line interferometers (12.5 GHz free-spectral range) to realize a high-rate entanglement source. The ability to resolve time-bin qubits into 80 ps wide bins is enabled by newly developed low-jitter differential superconducting nanowire single-photon detectors (SNSPDs) [22]. Wavelength multiplexing is used to realize multiple high visibility channel pairings which together sum to a high coincidence rate. Each of the pairings can be considered an independent carrier of photonic entanglement [23, 24] and therefore the system as a whole is applicable to flex-grid architectures through the use of wavelength selective switching [25, 26]. However, we focus on maximizing the rate between two receiving stations, Alice and Bob (Fig. 5.1a). Each station is equipped with a DWDM that separates the frequency multiplexed channel into multiple fibers for detection. The SNSPDs are used with a real-time pulse pileup and time-walk correction technique [27] to keep jitter low even at high count rates.

We quantify per-channel brightness and visibility as a function of pump power, as well as collection efficiencies, coincidence rates across 8 channel pairs. We show that the 8-channel system achieves visibilities that average to 99.3% at low mean

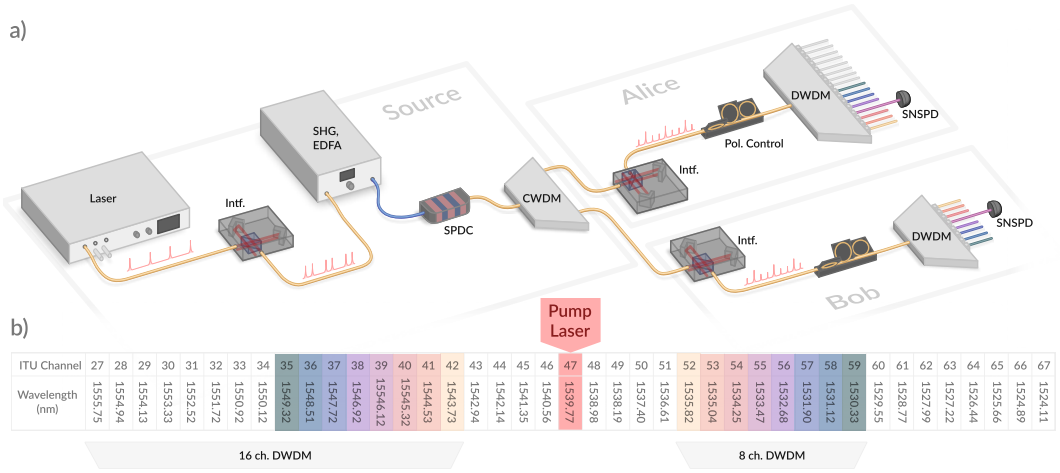

Figure 5.1: Experimental setup. a) Pulses from a 1539.47 nm mode locked laser (Pritel UOC) are split into two by an 80-ps delay-line interferometer before up-conversion and amplification in a second harmonic generation + erbium doped fiber amplifier (SHG + EDFA) module (Pritel). A short PM fiber from the SHG module connects to a nonlinear crystal generating photon pairs by spontaneous parametric down-conversion (SPDC). The coarse wavelength division multiplexing (CWDM) module separates the photon pair spectrum into eight 13 nm-wide bands around 1530 and 1550 nm, for the signal and idler photon, respectively. The signal and idler are directed to the Bob and Alice stations, respectively. The readout interferometers introduce the same time delay as the source interferometer. Polarization controllers are used to maximize the coincidence rates. 100 GHz spacing dense wavelength division multiplexer (DWDM) modules are used to direct each frequency channel into a distinct fiber. Two superconducting nanowire single photon detectors (SNSPDs) are used to measure a specific frequency multiplexed channel pair. Measurements for different multiplexed channels are performed in succession to resolve full system performance. b) ITU channels used in the experiment. Pairs of channels highlighted with the same color obey the phase and pump-energy matching condition for SPDC. To assess the full 16 channels (27-42) of Alice's DWDM multiplexer, Bob's 8-channel DWDM is replaced with a narrowband filter with tunable resonance frequency (not shown in figure).

photon number $\mu_L = 5.6{\times}10^5 \pm 9{\times}10^6$. At a higher power ($\mu_H = 5.0{\times}10^3 \pm 3{\times}10^4$), we demonstrate a total coincidence rate of 3.55 MHz with visibilities that average to 96.6%. Through quantum state tomography we bound the distillable entanglement rate of the system to between 69% and 91% of the μ_H coincidence rate (2.46 - 3.25 Mebits/s).

Quantifying a source's spectral mode purity is important for gauging its utility in advanced quantum networks that rely on interferometric measurements like two-photon interference which enables Bell-state measurements (BSM) [5]. With Schmidt decomposition we quantify the modal purity of single DWDM channel pairs and derive the inverse Schmidt number which serves as an estimate for two-photon interference visibility between two such sources. Ultimately, we demonstrate that an entanglement generation source of this design makes for a robust and powerful building block for future high-rate quantum networks.

5.2 System

Figure 5.1 shows the experimental setup. Pulses from the 4.09 GHz mode-locked laser, with a center wavelength at 1539.47 nm, are sent through an 80 ps delay-line interferometer (Optoplex DPSK Phase Demodulator). All interferometers used are the same type; they have insertion loss of 1.37 $\pm$ 0.29 dB, are polarization independent, and have extinction ratios greater than 18 dB. The source interferometer produces two pulses each clock cycle used to encode early/late basis states ($|e\rangle, |l\rangle$), which are subsequently up-converted by a second harmonic generation (SHG) module (Pritel) and down-converted into entangled photon pairs by a type-0 spontaneous parametric down conversion (SPDC) crystal (Covesion) [17]. The SPDC module uses a 1 cm long waveguide-coupled MgO-doped lithium niobate crystal with an 18.3 µ polling period. The up-converted pulses at 769 nm have a FWHM bandwidth of 243 GHz (0.48 nm), which along with the phase matching condition of the SPDC waveguide, defines a wide joint spectral intensity (JSI) function [28].

The photon pairs are separated by a coarse wavelength division multiplexer (CWDM) which serves to split the SPDC spectrum into two wide-bandwidth halves. For a system using more than 16 DWDM channels at Alice and Bob, the CWDM would be replaced with a splitter that efficiently sends the full SPDC spectrum shorter than 1540 nm to Bob, and the spectrum longer than 1540 nm to Alice. A dichroic splitter with a sharp transition at 1540 nm would also enable the use of DWDM channels 43-46 and 48-51. The pairs are of the form $|\psi\rangle = \frac{1}{\sqrt{2}}\left(|e\rangle_s|e\rangle_i + e^{i\phi}|l\rangle_s|l\rangle_i\right)$.

Entangled idler and signal photons are sent to the receiving stations labeled Alice and Bob, respectively. One readout interferometer at each station projects all spectral bands into a composite time-phase basis. From here, dense wavelength division multiplexers (DWDM) divide up the energy-time entangled photon pairs into spectral channels.

The DWDM outputs are sent to differential niobium nitride (NbN) single pixel SNSPDs [22] with 22 × 15 μm active areas formed by meanders of 100-nm-wide and 5-nm-thick niobium nitride (NbN) nanowires on a 500 nm pitch. These measure the arrival time of photons with respect to a clock signal derived from the mode locked laser. Use of the high system repetition rate and compact 80 ps delay interferometers is only possible due to the high timing resolution of these detectors. Low jitter performance is achieved by incorporating impedance matching tapers for efficient RF coupling, resulting in higher slew rate pulses, and by enabling RF pulse readout from both ends of the nanowire. The dual-ended readout allows for the cancellation of jitter caused by the variable location of photon arrival along the meander when the differential signals are recombined with a balun. SNSPDs of this type reach system jitters down to 13.0 ps FWHM, and 47.6 ps FW(1/100)M [22]. We use two SNSPDs for this demonstration with efficiencies at 1550 nm of 66% and 74%. They exhibit 3 dB maximum count rates of 15.1 and 16.0 MHz. A full 8-channel implementation of this system would require 16 detectors operating in parallel at both Alice and Bob. To read out both outputs of both interferometers, 4 detectors per channel are required, resulting in 32 detectors total.

In the following, rigorous tests of entanglement are primarily done with the 8 ITU 100 GHz channel pairings: Ch. 35-42 at Alice and Ch. 52-59 at Bob. However, the source brightness measurements were conducted on a partially realized 16-channel configuration which makes use of all 16 channels available on Alice's DWDM.

Signals from the SNSPDs are directed to a free-running time tagger (Swabian) and processed with custom software. The resulting histograms, referenced from a shared clock (Fig 5.2a), depict three peaks, which are caused by the sequential delays of the source and readout interferometers. Some intensity imbalance between long and short paths is present in these interferometers, which explains the asymmetry between early and late peaks in Fig. 5.2a. Such imbalances are present in both the source and readout interferometers to varying degrees. The interferometer used for the source exhibits an early/late intensity balance ratio of 1.13. Alice and Bob's interferometers exhibit early/late imbalances of 1.24 and 1.15, respectively. These

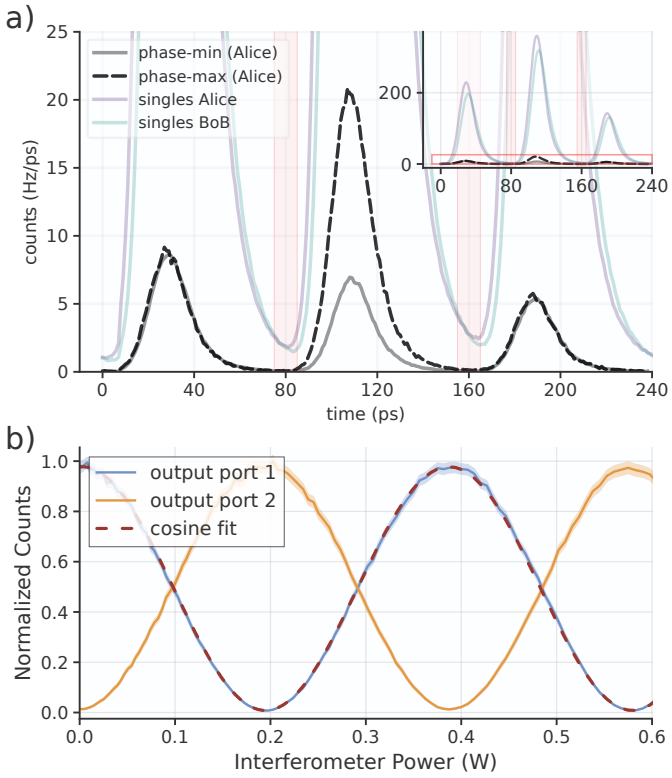

Figure 5.2: Entanglement visibility characterization. a) Histogram of photon arrival events with respect to the 4.09 GHz clock. Dashed black and grey lines show the response functions for coincidence events. Events within 10 ps guard regions centered at 80 and 160 ps (shaded red) are discarded for analysis of coincidences between individual bins. This is done to maximize visibility in the presence of some minor overlap of the pulses. The coincidence histograms include pairings from any combination of early, middle, and late time bins. Therefore, the height of the center peak in the phase-min state is not near zero, as non-phase-varying terms contribute. b) Coincidence rate interference fringes for the center time bin in isolation. Based on the good agreement between the fringe data and a cosine fit, we make subsequent tomographic measurements assuming that phase is linear with the electrical power applied to the interferometer phase shifter.

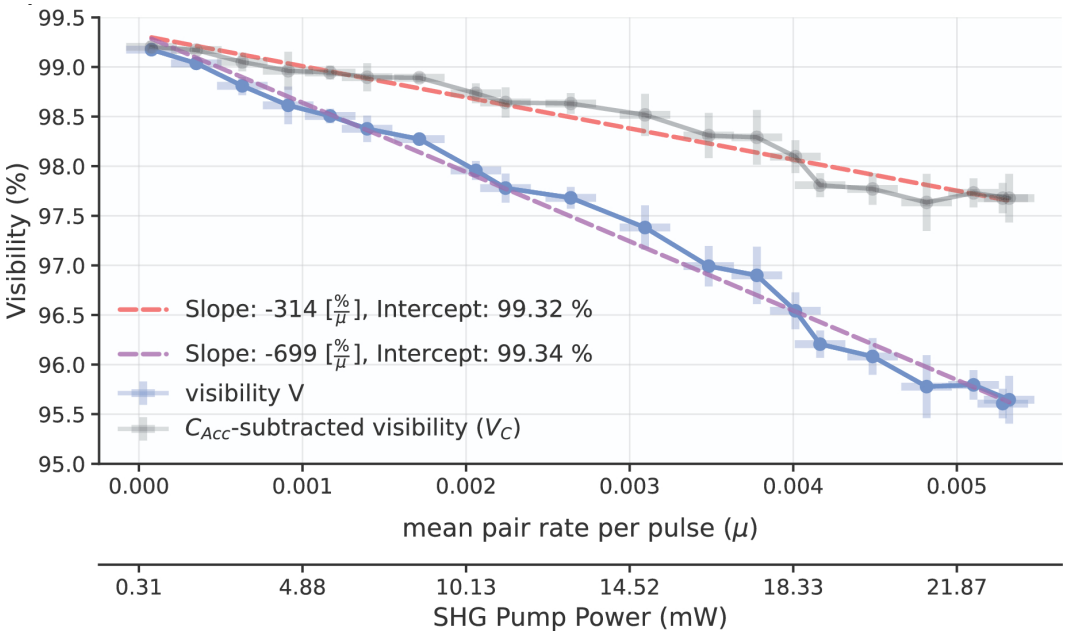

Figure 5.3: Entanglement visibility versus mean pair rate per pulse (μ) and SHG pump power. Error bars are calculated by taking multiple measurements of the center bin coincidence rate over some integration time. These measurements span small ranges of interferometer phase, as the extremum-finding algorithm jitters the interferometer voltage. V_C (grey data, red line) is a construction that models how visibility would be affected if accidental coincidences from mutually incompatible spectral modes could be mitigated in future systems.

induce imperfect overlap of certain time-bin modes of differing amplitudes. This mismatch lowers interference visibilities, see Section 5.4.

5.3 Results

The coincidence rate across Alice and Bob's middle bins varies sinusoidally with respect to the combined phase relationship of the source and readout interferometers [29, 17] (see Fig. 5.2b). In Fig. 5.2a the coincidences shown are for any combination of early, middle, or late bins. For tomography and visibility measurements, coincidence detections across specific bin pairings are considered.

Due to the small size (3×3 cm) and temperature insensitivity of the interferometers, minimal temporal phase drift is observed. Without active temperature control or phase feedback, we observe minimized coincidence rates of the center time bin stay within 6% of their original values after 50 minutes. Nevertheless, software is used to lock the voltage-controlled phase at a minimum or maximum with a

simple hill-climbing algorithm. This varies the phase by small amounts over several minutes to search for or maintain an extremum. This is simpler to implement than the techniques needed to stabilize interferometers of longer path length difference, including the use of precise temperature control [5] or co-propagating stabilization lasers [30].

Channels 35 and 59 are chosen for an analysis of entanglement visibility and rates versus pump power. Visibility with respect to pump power or mean entangled pair rate is shown in Fig. 5.3a. We define the entanglement visibility as $V = 100\% * (C_{max} - C_{min})/(C_{max} + C_{min})$ where C_{min} and C_{max} are the minimum and maximum coincidence rates in the middle bin for varied phase. As this coincidence rate depends on the total phase across the source and readout interferometers, only Bob's interferometer is actively controlled to scan the full state space.

The raw visibility versus μ is shown in blue in Fig. 5.3a. Relative to similar measurements [31], this drops quickly with increasing μ, and one reason is the presence of accidental coincidences across mutually incompatible spectral modes. The presence of these unwanted coincidences is a consequence of the narrowband filtering regime, and depends on factors included the singles rates S_A and S_B, and the geometric compensation factor δ. We model this type of accidental coincidence rate C_{Acc} versus μ, and subtract it off from coincidence measurements to produce the grey data in Fig. 5.3a. This simulated visibility's more gradual drop with increasing μ highlights the detrimental effect of our high single-to-coincidence rates S_A/C_{AB}, S_B/C_{AB}. As detailed in the Discussion section below, this motivates special source engineering techniques for future systems.

5.4 Impact of experimental imperfections

The experiment employs three Michelson interferometers with a path-length delay of 80 ps: one at the source to generate the early and late time-bins, and one prior to each detector to control the measurement basis. To determine the effect of interferometric imperfections on the entanglement visibility, we model the interferometers as equivalent Mach-Zehnder interferometers as shown in Fig. 5.4. Imperfections in the interferometer are captured by the transmittance t of the beamsplitter and internal path (mirror) efficiencies $|\alpha|^2$ and $|\beta|^2$. An ideal Michelson interferometer has $t = 1/\sqrt{2}$ and $|\alpha|^2 = |\beta|^2 = 1$.

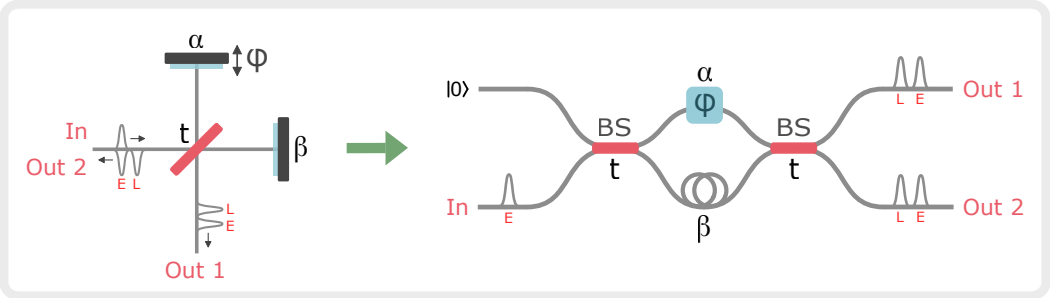

Figure 5.4: Model for Michelson interferometers employed in the experiment. The interferometer contains a beamsplitter with transmittance t and two mirrors with efficiencies α and β.

Source interferometer imperfections

In the experiment, pulses of coherent light from a mode-locked laser (MLL) are injected into the input of the source interferometer. A field $\hat{E}$ at the input of the source interferometer transforms as

$$\hat{E}_{\text{in}} \rightarrow rt\alpha e^{i\varphi}\hat{E}_{E,1} + r^2\alpha e^{i\varphi}\hat{E}_{E,2} + rt\beta\hat{E}_{L,1} + t^2\beta\hat{E}_{L,2} \tag{5.1}$$

$$+ ir\sqrt{1-|\alpha|^2}\hat{E}_{\text{vac}_1} + it\sqrt{1-|\beta|^2}\hat{E}_{\text{vac}_2} \tag{5.2}$$

where the early and late temporal modes are denoted by subscripts "E" and "L", the input and output modes are denoted by subscripts "in", "1" and "2", and $r = i\sqrt{1-|t|^2}$. Due to imperfect path efficiencies, part of the light leaks into the vacuum field mode $\hat{E}_{\text{vac}}$, which corresponds to the last term in Eq. 5.2. It follows that the power of the early and late output pulses in terms of the power of the input pulse are

$$P_{E,1} = |r|^2|t|^2|\alpha|^2P_{in}, \qquad P_{E,2} = |r|^4|\alpha|^2P_{in} \tag{5.3}$$

$$P_{L,1} = |r|^2|t|^2|\beta|^2P_{in}, \qquad P_{L,2} = |t|^4|\beta|^2P_{in}.$$

To generate the entangled photon pairs, one of the output ports of the source interferometer is up-converted by second harmonic generation (SHG) then down-converted via spontaneous parametric down conversion (SPDC), resulting in two-mode squeezed vacuum states (TMSVs) in early and late temporal modes with mean photon numbers μ_E and μ_L, respectively. The ratio of μ_E to μ_L depends on which output port of the source interferometer is used. Note that the definition of μ used in the main text is per source laser period or per experiment cycle (4.09 GHz). Therefore μ from the main text is equal to $\mu_E + \mu_L$. The output power of SHG

(P_{SHG}) as a function of the SHG pump power (P_p) is [32],

$$P_{SHG} = P_p \tanh^2 \sqrt{\eta_{SHG} P_p} \approx \eta_{SHG} P_p^2, \tag{5.4}$$

where η_{SHG} is the conversion efficiency of the SHG crystal. After SPDC, the squeezing parameter (ξ) of the TMSVs in terms of the SPDC pump power (P_{SHG}) is $\xi = \lambda\sqrt{P_{SHG}} \approx \lambda\sqrt{\eta_{SHG}} P_p$, where λ is proportional to the SPDC crystal length and nonlinear interaction strength [33]. The mean photon number in terms of the squeezing parameter is $\mu = \sinh^2 \xi \approx \xi^2$. Therefore, the mean photon numbers of the TMSVs as a function of the output pulses of the source interferometer are,

$$\mu_E \approx \lambda^2 \eta_{SHG} P_{E,i} \qquad\qquad \mu_L \approx \lambda^2 \eta_{SHG} P_{L,i}^2, \tag{5.5}$$

where $i = 1(2)$ corresponds to output port 1(2) of the source interferometer.

If output port 1 is used,

$$\mu_E/\mu_L \approx P_{E,1}^2/P_{L,1}^2 = |\alpha|^4/|\beta|^4,$$

whereas if output port 2 is used,

$$\mu_E/\mu_L \approx P_{E,2}^2/P_{L,2}^2 = |r|^8|\alpha|^4/|t|^8|\beta|^4.$$

When output port 1 of the source interferometer is used, if the internal path efficiencies of the source interferometer are different, there is an imbalance in the early and late mean photon numbers. When output port 2 is used, the effect of the imbalance in the internal path efficiencies on the ratio of early and late mean photon numbers can be compensated by imperfect transmittance: $\mu_E/\mu_L = 1$ when $|t|^2/|r|^2 = |\alpha|/|\beta|$.

Measurement interferometer imperfections

Imperfections in the measurement interferometers limit the entanglement visibility of the experiment. As described in the previous section, early and late TMSVs are generated by pumping the SPDC with early and late pulses. Each half of each TMSV is sent to a measurement interferometer (see Fig. 5.5). Let $|\xi\rangle$ denote the TMSV state,

$$|\xi\rangle = \sum_{n=0}^{\infty} (-1)^n \sqrt{\frac{\mu^n}{(1+\mu)^{n+1}}}\, |n_A, n_B\rangle\,, \tag{5.6}$$

where $|n_A, n_B\rangle$ denotes the state with n_A photons at the input of interferometer A and n_B photons at the input port of interferometer B. We model the input state to the

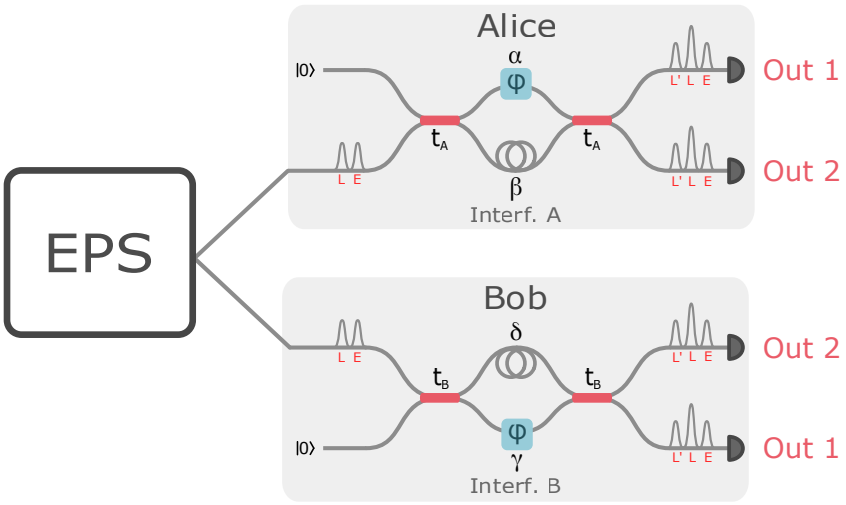

Figure 5.5: Setup for theoretical model of entanglement visibility experiment.

measurement interferometers as a product state of TMSV in early and late temporal modes, to lowest order in μ_E and μ_L:

$$\begin{aligned} |\Psi_{in}\rangle &= |\xi\rangle_E \otimes |\xi\rangle_L \\ &\approx \sqrt{1-(\mu_E+\mu_L)}\,|0,0\rangle_E\,|0,0\rangle_L \\ &\quad - \sqrt{\mu_E}\,|1,1\rangle_E\,|0,0\rangle_L - \sqrt{\mu_L}\,|0,0\rangle_E\,|1,1\rangle_L\,. \end{aligned} \tag{5.7}$$

We can express Eq. 5.7 in terms of the creation operators $\hat{a}^\dagger$ and $\hat{b}^\dagger$ of the field modes at the inputs of interferometers A and B, respectively:

$$|\Psi_{in}\rangle = \left(\sqrt{1-(\mu_E+\mu_L)} - \sqrt{\mu_E}\hat{a}_E^\dagger\hat{b}_E^\dagger - \sqrt{\mu_L}\hat{a}_L^\dagger\hat{b}_L^\dagger\right)|0,0\rangle_E\,|0,0\rangle_L\,. \tag{5.8}$$

Since the measurement interferometers are also Michelson interferometers, the

transformation relations are,

$$\hat{a}_E \mapsto r_A t_A \alpha e^{i\varphi} \hat{a}_{E,1} + r_A^2 \alpha e^{i\varphi} \hat{a}_{E,2} \tag{5.9}$$
$$+ r_A t_A \beta \hat{a}_{L,1} + t_A^2 \beta \hat{a}_{L,2} + c_A \hat{a}_{\mathrm{vac}_1} + d_A \hat{a}_{\mathrm{vac}_2},$$
$$\hat{b}_E \mapsto r_B t_B \gamma e^{i\varphi} \hat{b}_{E,1} + r_B^2 \gamma e^{i\varphi} \hat{b}_{E,2} \tag{5.10}$$
$$+ r_B t_B \delta \hat{b}_{L,1} + t_B^2 \delta \hat{b}_{L,2} + c_B \hat{b}_{\mathrm{vac}_1} + d_B \hat{b}_{\mathrm{vac}_2},$$
$$\hat{a}_L \mapsto r_A t_A \alpha e^{i\varphi} \hat{a}_{L,1} + r_A^2 \alpha e^{i\varphi} \hat{a}_{L,2} \tag{5.11}$$
$$+ r_A t_A \beta \hat{a}_{L',1} + t_A^2 \beta \hat{a}_{L',2} + c_A \hat{a}_{\mathrm{vac}_1} + d_A \hat{a}_{\mathrm{vac}_2},$$
$$\hat{b}_L \mapsto r_B t_B \gamma e^{i\varphi} \hat{b}_{L,1} + r_B^2 \gamma e^{i\varphi} \hat{b}_{L,2} \tag{5.12}$$
$$+ r_B t_B \delta \hat{b}_{L',1} + t_B^2 \delta \hat{b}_{L',2} + c_B \hat{b}_{\mathrm{vac}_1} + d_B \hat{b}_{\mathrm{vac}_2},$$
$$c_A = i r_A \sqrt{1 - |\alpha|^2}, \quad d_A = i t_A \sqrt{1 - |\beta|^2},$$
$$c_B = i r_B \sqrt{1 - |\delta|^2}, \quad d_B = i t_B \sqrt{1 - |\gamma|^2},$$

where L' denotes the temporal mode obtained by sending a photon in the late (L) mode through the long arm of an interferometer, and $\hat{a}_{\mathrm{vac}_i}$, $\hat{b}_{\mathrm{vac}_i}$ correspond to vacuum modes. To find the state at the output of the interferometers, we combine Eq. 5.8 with Eq. 5.9-5.12, and consider only terms relevant to post-selection on coincidences of the middle bins (L) of different interferometer outputs, to lowest order in μ_E and μ_L,

$$\begin{aligned}
|\Psi_{\mathrm{out}}\rangle &= r_A^* t_A r_B^* t_B \left(\beta\delta\sqrt{\mu_E} + \alpha\gamma\sqrt{\mu_L} e^{-2i\varphi}\right) |0,0;0,0\rangle_E \, |1,0;1,0\rangle_L \, |0,0;0,0\rangle_{L'} \\
&+ r_A^* t_A \left(t_B^2 \beta\delta\sqrt{\mu_E} + (r_B^*)^2 \alpha\gamma\sqrt{\mu_L} e^{-2i\varphi}\right) |0,0;0,0\rangle_E \, |1,0;0,1\rangle_L \, |0,0;0,0\rangle_{L'} \\
&+ r_B^* t_B \left(t_A^2 \beta\delta\sqrt{\mu_E} + (r_A^*)^2 \alpha\gamma\sqrt{\mu_L} e^{-2i\varphi}\right) |0,0;0,0\rangle_E \, |0,1;1,0\rangle_L \, |0,0;0,0\rangle_{L'} \\
&+ \left(t_A^2 t_B^2 \beta\delta\sqrt{\mu_E} + (r_A^*)^2 (r_B^*)^2 \alpha\gamma\sqrt{\mu_L} e^{-2i\varphi}\right) |0,0;0,0\rangle_E \, |0,1;0,1\rangle_L \, |0,0;0,0\rangle_{L'} \\
&+ \cdots
\end{aligned} \tag{5.13}$$

where $\left|n_{A,1}, n_{A_2}; n_{B_1}, n_{B,2}\right\rangle$ denotes the state with $n_{A,1}$ photons at output 1 of interferometer A, $n_{A,2}$ photons at output 2 of interferometer A, $n_{B,1}$ photons at output 1 of interferometer B, and $n_{B,2}$ photons at output 2 of interferometer B. We define the following parameters to simplify notation:

$$x \equiv \frac{\mu_E}{\mu_L}, \qquad \kappa_A \equiv \frac{|\beta|^2}{|\alpha|^2}, \qquad \kappa_B \equiv \frac{|\gamma|^2}{|\delta|^2}, \tag{5.14}$$

$$\epsilon_A = \frac{|t_A|^2}{|r_A|^2}, \qquad \epsilon_B \equiv \frac{|t_B|^2}{|r_B|^2}. \tag{5.15}$$

From Eq. 5.13, it follows that the coincidence probabilities for each combination of output ports are proportional to,

$$C_{A_1,B_1}(\varphi) \propto \sqrt{\frac{\kappa_B}{\kappa_A}} + \sqrt{\frac{\kappa_A}{\kappa_B}}x + 2\sqrt{x}\cos 2\varphi, \tag{5.16}$$

$$C_{A_1,B_2}(\varphi) \propto \frac{1}{\epsilon_B}\sqrt{\frac{\kappa_B}{\kappa_A}} + \epsilon_B\sqrt{\frac{\kappa_A}{\kappa_B}}x + 2\sqrt{x}\cos 2\varphi, \tag{5.17}$$

$$C_{A_2,B_1}(\varphi) \propto \frac{1}{\epsilon_A}\sqrt{\frac{\kappa_B}{\kappa_A}} + \epsilon_A\sqrt{\frac{\kappa_A}{\kappa_B}}x + 2\sqrt{x}\cos 2\varphi, \tag{5.18}$$

$$C_{A_2,B_2}(\varphi) \propto \frac{1}{\epsilon_A\epsilon_B}\sqrt{\frac{\kappa_B}{\kappa_A}} + \epsilon_A\epsilon_B\sqrt{\frac{\kappa_A}{\kappa_B}}x + 2\sqrt{x}\cos 2\varphi, \tag{5.19}$$

where the phase factors in the reflectivities r_A, r_B are absorbed into the definition of φ. Therefore, the entanglement visibilities, $V = \frac{\max(C(\varphi))-\min(C(\varphi))}{\max(C(\varphi))+\min(C(\varphi))}$, for each combination of output ports are:

$$V_{A_1,B_1} = \frac{2\sqrt{x}}{\sqrt{\frac{\kappa_B}{\kappa_A}} + \sqrt{\frac{\kappa_A}{\kappa_B}}x}, \tag{5.20}$$

$$V_{A_1,B_2} = \frac{2\sqrt{x}}{\frac{1}{\epsilon_B}\sqrt{\frac{\kappa_B}{\kappa_A}} + \epsilon_B\sqrt{\frac{\kappa_A}{\kappa_B}}x}, \tag{5.21}$$

$$V_{A_2,B_1} = \frac{2\sqrt{x}}{\frac{1}{\epsilon_A}\sqrt{\frac{\kappa_B}{\kappa_A}} + \epsilon_A\sqrt{\frac{\kappa_A}{\kappa_B}}x}, \tag{5.22}$$

$$V_{A_2,B_2} = \frac{2\sqrt{x}}{\frac{1}{\epsilon_A\epsilon_B}\sqrt{\frac{\kappa_B}{\kappa_A}} + \epsilon_A\epsilon_B\sqrt{\frac{\kappa_A}{\kappa_B}}x}. \tag{5.23}$$

Unity visibility is achievable for each combination of output ports: $V_{A_1,B_1} = 1$ when $x = \kappa_B/\kappa_A$, $V_{A_1,B_2} = 1$ when $x = \kappa_B/(\kappa_A\epsilon_B^2)$, $V_{A_2,B_1} = 1$ when $x = \kappa_B/(\kappa_A\epsilon_A^2)$, and $V_{A_2,B_2} = 1$ when $x = \kappa_B/(\kappa_A\epsilon_A^2\epsilon_B^2)$. Therefore, the effect of imbalances in the source and measurement interferometers is to shift the optimal ratio of early to late mean photon numbers. Imbalances in the measurement interferometers can be compensated by imbalances in the source interferometer in order to obtain unity visibility. Moreover, in the single photon limit, the visibility is insensitive to the absolute path efficiencies in the experiment. The visibility depends only on the ratio of path efficiencies between the measurement interferometers (κ_A/κ_B). The entanglement visibilities for each combination of output ports as a function of

$x = \mu_E/\mu_L$ for various ratios of interferometric path efficiencies are shown in Fig. 5.6.

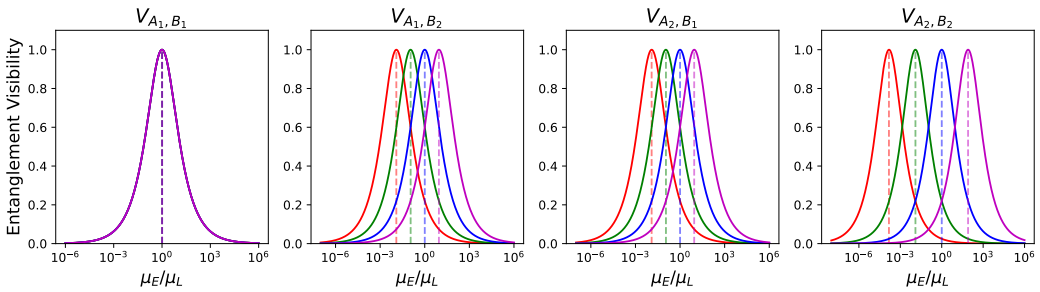

Figure 5.6: Entanglement visibility as function of μ_E/μ_L for fixed $\kappa_B/\kappa_A = 1$ and $\epsilon_A = \epsilon_B = 90/10$ (red), $75/25$ (blue), $50/50$ (green), $25/75$ (purple).

Multiphoton effects

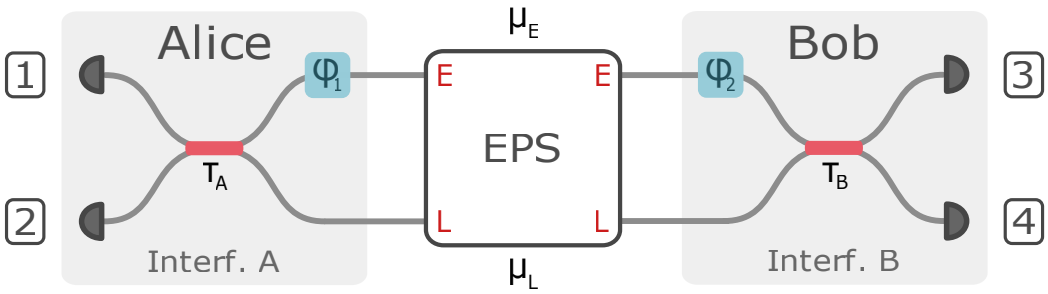

Figure 5.7: Setup for phase space modeling of entanglement visibility experiment.

Calculating the entanglement visibility to higher order photon number contributions quickly becomes intractable with the Fock space approach in the previous section. To study the effect of multiphoton events on the entanglement visibility, we model the experiment using phase space methods based on a characteristic function formalism [34, 35]. The model setup is shown in Fig 5.7. As in the Fock space approach, the input state is modeled as a product state of TMSV in early and late temporal modes, with mean photon numbers μ_E and μ_L, respectively. The measurement interferometers are modeled as beamsplitters in the temporal domain that mix the early and late input modes with transmittances τ_A and τ_B, which absorb the interferometric path efficiencies and spatial beamsplitter transmittances. Since the input state is modeled as a Gaussian state, and the measurement interferometers are modeled as Gaussian operations, we can find the symplectic transformation that maps the characteristic function of the input state to that of the state prior to detection.

Following Ref. [36], the characteristic function for an N-mode bosonic state is

$$\chi(\xi) = \mathrm{Tr}\left[\hat{\rho}\exp(-i(\hat{x}_1, \hat{p}_1, \hat{x}_2, \hat{p}_2, \cdots \hat{x}_N, \hat{p}_N)\xi)\right] \tag{5.24}$$

where $\xi \in \mathbb{R}^{2N}$, ρ is the density matrix, and $\hat{x}_i = \frac{1}{\sqrt{2}}(\hat{a}_i^\dagger + \hat{a}_i)$ and $\hat{p}_i = \frac{1}{\sqrt{2}}(\hat{a}_i^\dagger + \hat{a}_i)$ are the quadrature operators for mode i with annihilation operator $\hat{a}_i$. A Gaussian state is a state whose characteristic function that takes a Gaussian form,

$$\chi(\xi) = \exp\left(-\frac{1}{4}\xi^T\gamma\xi - id^T\xi\right), \tag{5.25}$$

which is fully characterized by the displacement vector d and covariance matrix γ, i.e., the first and second moments. For the TMSV state, the displacement vector is the null vector $d = (0, 0, 0, 0)$ and the covariance matrix is given by,

$$\gamma_{TMSV}(\mu) = \begin{pmatrix} \mathbf{A} & \mathbf{B} \\ \mathbf{B} & \mathbf{A} \end{pmatrix}, \quad \mathbf{A} = \begin{pmatrix} 1+2\mu & 0 \\ 0 & 1+2\mu \end{pmatrix}, \tag{5.26}$$

$$\mathbf{B} = \begin{pmatrix} 2\sqrt{\mu(\mu+1)} & 0 \\ 0 & -2\sqrt{\mu(\mu+1)} \end{pmatrix}, \tag{5.27}$$

where $\gamma_{TMSV}(\mu)$ is written in block matrix form. Therefore, the covariance matrix for the input state of our experiment is,

$$\gamma_{in}(\mu_E, \mu_L) = \gamma_{TMSV}(\mu_E) \oplus \gamma_{TMSV}(\mu_L). \tag{5.28}$$

The characteristic function of the input state is mapped to the characteristic function of the state prior to detection by a symplectic transformation,

$$\chi_{in}(\xi) = \exp\left(-\frac{1}{4}\xi^T\gamma_{in}\xi\right) \mapsto \chi_{out}(\xi) = \exp\left(-\frac{1}{4}\xi^T S^T\gamma_{in}S\xi\right), \tag{5.29}$$

where S is the Symplectic matrix of the interferometers. We construct S from the Symplectic matrices of the phase shifter (S_{PS}) and beamsplitter (S_{BS}) [35],

$$S_{PS}(\varphi) = \begin{pmatrix} \cos\varphi & \sin\varphi \\ -\sin\varphi & \cos\varphi \end{pmatrix}, \tag{5.30}$$

$$S_{BS}(\tau) = \begin{pmatrix} \mathbf{T} & \mathbf{R} \\ \mathbf{R} & \mathbf{T} \end{pmatrix}, \quad \mathbf{T} = \begin{pmatrix} \tau & 0 \\ 0 & \tau \end{pmatrix}, \quad \mathbf{R} = \begin{pmatrix} 0 & -\sqrt{1-\tau^2} \\ \sqrt{1-\tau^2} & 0 \end{pmatrix}. \tag{5.31}$$

From the output characteristic function χ_{out}, we obtain the coincidence probabilities using Eq. 9 of Ref. [36],

$$\mathrm{Tr}\left[\hat{\rho}_{\mathrm{out}}\hat{\Pi}\right] = \left(\frac{1}{2\pi}\right)^N \int dx^{2N}\chi_{\mathrm{out}}(x)\chi_{\Pi}(-x), \tag{5.32}$$

where $\hat{\rho}_{\text{out}}$ is the state prior to detection with characteristic function χ_{out}, and $\hat{\Pi}$ is the measurement operator corresponding to coincidences between detectors from different interferometers. The measurement operators for a threshold detector, which distinguishes between a detection event (at least one photon) and no detection event (zero photons), are,

$$\hat{\Pi}_{\text{event}} = \hat{I} - |0\rangle\langle 0|, \quad \hat{\Pi}_{\text{no event}} = |0\rangle\langle 0|, \tag{5.33}$$

where $\hat{I}$ is the 2 by 2 identity matrix. The measurement operator for coincidences between, e.g., detectors 1 and 4 are,

$$\hat{\Pi}_{1,4} = \hat{\Pi}_{\text{event},1} \otimes \hat{I}_2 \otimes \hat{I}_3 \otimes \hat{\Pi}_{\text{event},4}, \tag{5.34}$$

where the subscripts denote the output modes labeled in Fig. 5.7. We derive an analytical expression for the coincidence probability, $C(\varphi) = \text{Tr}\left[\hat{\rho}_{\text{out}}\hat{\Pi}_{1,4}\right]$, that encompasses all multiphoton contributions,

$$C(\varphi) = 1 - \frac{1}{|f(\mu_E, \mu_L, \tau_A)|} - \frac{1}{|g(\mu_E, \mu_L, \tau_B)|} + \frac{1}{|h(\mu_E, \mu_L, \tau_A, \tau_B, \varphi)|}, \tag{5.35}$$

$$f(\mu_E, \mu_L, \tau_A) = 1 + \mu_L + \tau_A(\mu_E - \mu_L), \tag{5.36}$$

$$g(\mu_E, \mu_L, \tau_B) = 1 + \mu_E + \tau_B(\mu_L - \mu_E), \tag{5.37}$$

$$\begin{aligned} h(\mu_E, \mu_L, \tau_A, \tau_B) = {} & 1 + \mu_E + \mu_L(1 + \mu_E)(1 - \tau_A) \\ & - \mu_E\tau_B(1 + \mu_L) + \tau_A\tau_B(\mu_E + \mu_L + 2\mu_E\mu_L) \\ & - 2\sqrt{\mu_E\mu_L\tau_A(1 + \mu_E)(1 + \mu_L)(1 - \tau_A)}\sqrt{\tau_B(1 - \tau_B)}\cos\varphi, \end{aligned} \tag{5.38}$$

where $\varphi = \varphi_A - \varphi_B$ is the relative phase between interferometers A and B. The different visibilities in each output port combination as a result of interferometric imbalances can be obtained by adjusting τ accordingly. To isolate the impact of multiphoton contributions to the visibility, we set $\tau_A = \tau_B = \frac{1}{\sqrt{2}}$, and obtain the following expression for the entanglement visibility, $V(\mu_E, \mu_L) = \frac{C(0) - C(\pi)}{C(0) + C(\pi)}$:

$$V(\mu_E, \mu_L) = \frac{2/\sqrt{G_-(\mu_E, \mu_L)} - 2/\sqrt{G_+(\mu_E, \mu_L)}}{1 - 4/(2 + \mu_E + \mu_L) + 2/\sqrt{G_-(\mu_E, \mu_L)} + 2/\sqrt{G_+(\mu_E, \mu_L)}}, \tag{5.39}$$

$$
\begin{aligned}
G_{\pm}(\mu_E,\mu_L) = {} & \mu_E^2(9+8\mu_L(2+\mu_L)) \\
& \pm (4+3\mu_L)\left(\pm 4 \pm 3\mu_L + 4\sqrt{\mu_E\mu_L(1+\mu_E)(1+\mu_L)}\right) \\
& + 2\mu_E\left(12 \pm 6\sqrt{\mu_E\mu_L(1+\mu_E)(1+\mu_L)}\right) \\
& + 2\mu_E\mu_L\left(19+8\mu_L \pm 4\sqrt{\mu_E\mu_L(1+\mu_E)(1+\mu_L)}\right).
\end{aligned} \tag{5.40}
$$

By expanding Eq. 5.39 to first order in μ_E and μ_L,

$$
V(\mu_E,\mu_L) = \frac{2\sqrt{\frac{\mu_E}{\mu_L}}}{1+\frac{\mu_E}{\mu_L}} - \frac{\mu_E}{\mu_L}\frac{\left(5(\frac{\mu_E}{\mu_L}+\frac{\mu_L}{\mu_E})+6\right)}{2(1+\frac{\mu_E}{\mu_L})^2}\sqrt{\mu_E\mu_L} + \cdots \tag{5.41}
$$

we see that the first term matches Eq. 5.20-5.23 for $t_A = t_B = \frac{1}{\sqrt{2}}$, $\beta/\alpha = \gamma/\delta = 1$. Moreover, for $\mu_{eq} \equiv \mu_E = \mu_L$, Eq. 5.41 reduces to $V(\mu_{eq}) = 1 - 2\mu_{eq}$. Thus, the upper bound on the visibility is set by the mean photon number, i.e., multiphoton effects. Entanglement visibilities of more than 90% are possible when $0.39 < \mu_E/\mu_L < 2.55$ and $\mu_L < 0.0.056$. The entanglement visibility $V(\mu_E,\mu_L)$ in Eq. 5.39 is plotted for various mean photon numbers in Fig. 5.8.

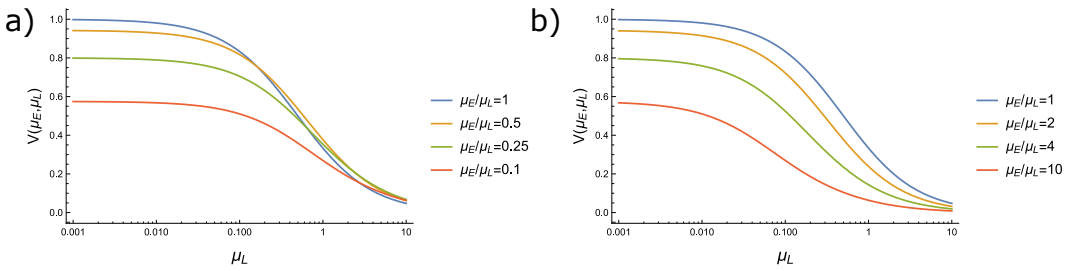

Figure 5.8: Entanglement visibility as a function of mean photon number for a) $\mu_E/\mu_L \geq 1$ and b) $\mu_E/\mu_L \leq 1$ with $\tau_A = \tau_B = 1/\sqrt{2}$.

5.5 Discussion

We have demonstrated that a time-bin entanglement source based on a mode-locked laser, spectral multiplexing and low-jitter detectors produces high entangled photon rates suitable for QKD or advanced quantum networks. The distillable entanglement rate, achievable secret key rate, and visiblilities of this source are highly competitive relative to other multiplexed entanglement distribution systems [10, 9, 31, 24, 23]. Still, there is potential to increase rates beyond those measured here with some straightforward changes to the setup. First, a higher power EDFA-amplified SHG

rate metric (μ at max)	1 Channel	8 Channels	16 Channels	60 Channels
coincidence rate, C_{AB} (0.014)	0.755	5.41	11.6	34.9
log negativity, C_N (0.010)	0.600	4.30	9.19	27.7
coherent info., C_I (0.006)	0.345	2.47	5.28	15.9
secret key rate, SKR (0.007)	0.309	2.21	4.73	14.3

Table 5.1: Per-channel predicted maximum values for the 4 rate metrics are shown in the '1 Channel' column. Depending on the metric, the maxima are achieved for different pump powers μ. The μ value that maximizes each metric is shown in parenthesis on the left.

module or tapered amplifier may be used. With this, we predict a single channel pair could sustain rates up to those specified in the first column of Table 5.1. These metrics all depend on both entanglement quality and coincidence rate C_{AB}. Due to the trade-off between C_{AB} and entanglement quality or visibility, they all reach maximum values for particular pump powers. Our measurements of 8 channel and 16 channel configurations imply the approximately multiplicative scalings in columns 2 and 3 of Table 5.1, as coincidence rates of these channels pairs are all withing 27% of each other. From measurements of the SPDC spectrum, it is also possible to extrapolate rates to a 60-channel 100 GHz DWDM configuration that includes channels spanning the L, C, and S ITU bands. This configuration could sustain 34.9 MHz total coincidence rate, and a distillable entanglement rate between 27.7 (C_N) and 15.9 Mebits/s (C_I). These rates are impressive considering they are achievable with existing SNSPDs and other technology.

The ratio of singles rates S_A, S_B to coincidence rates C_{AB} are high in this system due to the relatively wide-band JSI and narrow filters. Each DWDM channel at Alice picks up a large fraction of photons that can't be matched with pairs passing though the corresponding channel passband at Bob, a feature quantified by the δ factor. The high singles rates lead to accidental coincidences from mutually incompatible spectral modes that lower visibility and load the detectors with useless counts. However, there is potential to mitigate these extra counts by embedding the nonlinear crystal undergoing SPDC in a cavity that enhances emission at the center frequencies of multiple DWDM channels [37, 38, 39]. Also, there are other approaches to achieving such intensity islands that require dispersion engineering [40, 41]. With such periodically enhanced emission, the resulting JSI would exhibit a series of intensity islands lying along the energy-matching anti-diagonal, easily

separable with DWDMs at Alice and Bob. The photon flux for each each channel would originate primarily from these islands covered by both signal and idler DWDM passbands, resulting in a higher ratio of coincidences to singles. The probability of accidental coincidences C_{Acc} would be lower, and therefore bring the decrease of visibility with μ more in line with the modeled V_C data in Fig. 5.3. We intend for the V_C construction to represent how visibility would degrade primarily due to multi-pair effects, assuming accidental coincidences from incompatible spectral modes could be mitigated. The more gradual decrease in visibility with μ would enable substantially higher maximum rate metrics than those in Table 5.1.

This source is a fundamental building block for future space-to-ground and ground-based quantum networks. It leverages the strengths of the latest SNSPD developments–namely simultaneous high count rates, low jitter and high efficiency–and in doing so adopts interferometers and DWDM systems that are compact, stable and accessible. By elevating the system clock rate to 4.09 GHz and shrinking the time bin size to 80 ps, we have demonstrated a new state of the art in quantum communication that enables adoption of mature and extensively developed technologies from classical optical networks. Also, the spectral multiplexing methods used here are potentially compatible with those demonstrated in broadband quantum memories [42] and optical quantum computing [43].

References

[1] Peter W. Shor. "Polynomial-Time Algorithms for Prime Factorization and Discrete Logarithms on a Quantum Computer." In: SIAM Journal on Computing 26.5 (1997), pp. 1484–1509. DOI: 10.1137/S0097539795293172. eprint: https://doi.org/10.1137/S0097539795293172. URL: https://doi.org/10.1137/S0097539795293172.

[2] Michael A. Nielsen and Isaac L. Chuang. Quantum computation and quantum information. Cambridge university press, 2010.

[3] Stephanie Wehner, David Elkouss, and Ronald Hanson. "Quantum internet: A vision for the road ahead." In: Science 362.6412 (2018), eaam9288.

[4] Charles H. Bennett, Gilles Brassard, Claude Crépeau, Richard Jozsa, Asher Peres, and William K. Wootters. "Teleporting an unknown quantum state via dual classical and Einstein-Podolsky-Rosen channels." In: Phys. Rev. Lett. 70 (13 Mar. 1993), pp. 1895–1899. DOI: 10.1103/PhysRevLett.70.1895. URL: https://link.aps.org/doi/10.1103/PhysRevLett.70.1895.

[5] Raju Valivarthi, Samantha I. Davis, Cristián Peña, et al. "Teleportation Systems Toward a Quantum Internet." In: PRX Quantum 1 (2 Dec. 2020), p. 020317. DOI:

10.1103/PRXQuantum.1.020317. URL: https://link.aps.org/doi/10.1103/PRXQuantum.1.020317.

[6] Jian-Wei Pan, Dirk Bouwmeester, Harald Weinfurter, and Anton Zeilinger. "Experimental Entanglement Swapping: Entangling Photons That Never Interacted." In: Phys. Rev. Lett. 80 (18 May 1998), pp. 3891–3894. DOI: 10.1103/PhysRevLett.80.3891. URL: https://link.aps.org/doi/10.1103/PhysRevLett.80.3891.

[7] S. L. N. Hermans, M. Pompili, H. K. C. Beukers, S. Baier, J. Borregaard, and R. Hanson. "Qubit teleportation between non-neighbouring nodes in a quantum network." In: Nature 605.7911 (May 2022), pp. 663–668. ISSN: 1476-4687. DOI: 10.1038/s41586-022-04697-y. URL: https://doi.org/10.1038/s41586-022-04697-y.

[8] Yoann Pelet, Grégory Sauder, Mathis Cohen, Laurent Labonté, Olivier Alibart, Anthony Martin, and Sébastien Tanzilli. "Operational entanglement-based quantum key distribution over 50 km of real-field optical fibres." In: arXiv:2207.14707 (2022). URL: https://arxiv.org/abs/2207.14707.

[9] Muneer Alshowkan, Joseph M. Lukens, Hsuan-Hao Lu, Brian T. Kirby, Brian P. Williams, Warren P. Grice, and Nicholas A. Peters. "Broadband polarization-entangled source for C+L-band flex-grid quantum networks." In: Opt. Lett. 47.24 (Dec. 2022), pp. 6480–6483. DOI: 10.1364/OL.471363. URL: https://opg.optica.org/ol/abstract.cfm?URI=ol-47-24-6480.

[10] Sebastian Philipp Neumann, Mirela Selimovic, Martin Bohmann, and Rupert Ursin. "Experimental entanglement generation for quantum key distribution beyond 1 Gbit/s." In: Quantum 6 (Sept. 2022), p. 822. ISSN: 2521-327X. DOI: 10.22331/q-2022-09-29-822. URL: https://doi.org/10.22331/q-2022-09-29-822.

[11] Simone Atzeni, Adil S. Rab, Giacomo Corrielli, Emanuele Polino, Mauro Valeri, Paolo Mataloni, Nicolò Spagnolo, Andrea Crespi, Fabio Sciarrino, and Roberto Osellame. "Integrated sources of entangled photons at the telecom wavelength in femtosecond-laser-written circuits." In: Optica 5.3 (2018), pp. 311–314.

[12] Chang-Wei Sun, Su-Heng Wu, Jia-Chen Duan, Jian-Wei Zhou, Jun-Lei Xia, Ping Xu, Zhenda Xie, Yan-Xiao Gong, and Shi-Ning Zhu. "Compact polarization-entangled photon-pair source based on a dual-periodically-poled Ti: LiNbO 3 waveguide." In: Optics letters 44.22 (2019), pp. 5598–5601.

[13] Wen-Zhao Liu, Ming-Han Li, Sammy Ragy, Si-Ran Zhao, Bing Bai, Yang Liu, Peter J Brown, Jun Zhang, Roger Colbeck, Jingyun Fan, et al. "Device-independent randomness expansion against quantum side information." In: Nature Physics 17.4 (2021), pp. 448–451.

[14] Florian Kaiser, Lutfi Arif Ngah, Amandine Issautier, Tom Delord, Djeylan Aktas, MP De Micheli, A Kastberg, L Labonté, O Alibart, A Martin, et al. "Polarization entangled photon-pair source based on quantum nonlinear photonics and interferometry." In: Optics Communications 327 (2014), pp. 7–16.

[15] Ali Anwar, Chithrabhanu Perumangatt, Fabian Steinlechner, Thomas Jennewein, and Alexander Ling. "Entangled photon-pair sources based on three-wave mixing in bulk crystals." In: Review of Scientific Instruments 92.4 (2021).

[16] Sebastian Philipp Neumann, Thomas Scheidl, Mirela Selimovic, Matej Pivoluska, Bo Liu, Martin Bohmann, and Rupert Ursin. "Model for optimizing quantum key distribution with continuous-wave pumped entangled-photon sources." In: Physical Review A 104.2 (2021), p. 022406.

[17] I. Marcikic, H. de Riedmatten, W. Tittel, V. Scarani, H. Zbinden, and N. Gisin. "Time-bin entangled qubits for quantum communication created by femtosecond pulses." In: Phys. Rev. A 66 (6 Dec. 2002), p. 062308. DOI: 10.1103/PhysRevA.66.062308. URL: https://link.aps.org/doi/10.1103/PhysRevA.66.062308.

[18] Dong-Dong Li, Song Gao, Guo-Chun Li, et al. "Field implementation of long-distance quantum key distribution over aerial fiber with fast polarization feedback." In: Opt. Express 26.18 (Sept. 2018), pp. 22793–22800. DOI: 10.1364/OE.26.022793. URL: https://opg.optica.org/oe/abstract.cfm?URI=oe-26-18-22793.

[19] Erik Fitzke, Lucas Bialowons, Till Dolejsky, Maximilian Tippmann, Oleg Nikiforov, Thomas Walther, Felix Wissel, and Matthias Gunkel. "Scalable Network for Simultaneous Pairwise Quantum Key Distribution via Entanglement-Based Time-Bin Coding." In: PRX Quantum 3 (2 May 2022), p. 020341. DOI: 10.1103/PRXQuantum.3.020341. URL: https://link.aps.org/doi/10.1103/PRXQuantum.3.020341.

[20] Jeongwan Jin, Jean-Philippe Bourgoin, Ramy Tannous, Sascha Agne, Christopher J. Pugh, Katanya B. Kuntz, Brendon L. Higgins, and Thomas Jennewein. "Genuine time-bin-encoded quantum key distribution over a turbulent depolarizing free-space channel." In: Opt. Express 27.26 (Dec. 2019), pp. 37214–37223. DOI: 10.1364/OE.27.037214. URL: https://opg.optica.org/oe/abstract.cfm?URI=oe-27-26-37214.

[21] Christoph Simon, Mikael Afzelius, Jürgen Appel, A. Boyer de La Giroday, S. J. Dewhurst, Nicolas Gisin, C. Y. Hu, F. Jelezko, Stefan Kröll, J. H. Müller, et al. "Quantum memories: a review based on the European integrated project "qubit applications (QAP)"." In: The European Physical Journal D 58 (2010), pp. 1–22.

[22] Marco Colangelo, Boris Korzh, Jason P. Allmaras, et al. "Impedance-Matched Differential Superconducting Nanowire Detectors." In: Phys. Rev. Appl. 19 (4 Apr. 2023), p. 044093. DOI: 10.1103/PhysRevApplied.19.044093. URL: https://link.aps.org/doi/10.1103/PhysRevApplied.19.044093.

[23] Djeylan Aktas, Bruno Fedrici, Florian Kaiser, Tommaso Lunghi, Laurent Labonté, and Sébastien Tanzilli. "Entanglement distribution over 150 km in wavelength division multiplexed channels for quantum cryptography." In: Laser & Photonics Reviews 10.3 (2016), pp. 451–457. DOI: https://doi.org/10.1002/lpor.201500258. eprint: https://onlinelibrary.wiley.com/doi/pdf/10.1002/lpor.201500258. URL: https://onlinelibrary.wiley.com/doi/abs/10.1002/lpor.201500258.

[24] Sören Wengerowsky, Siddarth Koduru Joshi, Fabian Steinlechner, Hannes Hübel, and Rupert Ursin. "An entanglement-based wavelength-multiplexed quantum communication network." In: Nature 564.7735 (2018), pp. 225–228.

[25] Félicien Appas, Florent Baboux, Maria I. Amanti, Aristide Lemaítre, Fabien Boitier, Eleni Diamanti, and Sara Ducci. "Flexible entanglement-distribution network with an AlGaAs chip for secure communications." In: npj Quantum Information 7.1 (July 2021), p. 118. ISSN: 2056-6387. DOI: 10.1038/s41534-021-00454-7. URL: https://doi.org/10.1038/s41534-021-00454-7.

[26] Muneer Alshowkan, Philip G. Evans, Brian P. Williams, Nageswara S. V. Rao, Claire E. Marvinney, Yun-Yi Pai, Benjamin J. Lawrie, Nicholas A. Peters, and Joseph M. Lukens. "Advanced architectures for high-performance quantum networking." In: J. Opt. Commun. Netw. 14.6 (June 2022), pp. 493–499. DOI: 10.1364/JOCN.450201. URL: https://opg.optica.org/jocn/abstract.cfm?URI=jocn-14-6-493.

[27] Andrew Mueller, Emma E. Wollman, Boris Korzh, Andrew D. Beyer, Lautaro Narvaez, Ryan Rogalin, Maria Spiropulu, and Matthew D. Shaw. "Time-walk and jitter correction in SNSPDs at high count rates." In: Applied Physics Letters 122.4 (Jan. 2023). 044001. ISSN: 0003-6951. DOI: 10.1063/5.0129147. eprint: https://pubs.aip.org/aip/apl/article-pdf/doi/10.1063/5.0129147/16690545/044001_1_online.pdf. URL: https://doi.org/10.1063/5.0129147.

[28] Yoon-Ho Kim and Warren P. Grice. "Measurement of the spectral properties of the two-photon state generated via type II spontaneous parametric downconversion." In: Optics Letters 30.8 (2005), pp. 908–910.

[29] Takahiro Inagaki, Nobuyuki Matsuda, Osamu Tadanaga, Masaki Asobe, and Hiroki Takesue. "Entanglement distribution over 300 km of fiber." In: Opt. Express 21.20 (Oct. 2013), pp. 23241–23249. DOI: 10.1364/OE.21.023241. URL: https://opg.optica.org/oe/abstract.cfm?URI=oe-21-20-23241.

[30] P. Toliver, J. M. Dailey, A. Agarwal, and N. A. Peters. "Continuously active interferometer stabilization and control for time-bin entanglement distribution." In: Opt. Express 23.4 (Feb. 2015), pp. 4135–4143. DOI: 10.1364/OE.23.004135. URL: https://opg.optica.org/oe/abstract.cfm?URI=oe-23-4-4135.

[31] Jin-Hun Kim, Jin-Woo Chae, Youn-Chang Jeong, and Yoon-Ho Kim. "Quantum communication with time-bin entanglement over a wavelength-multiplexed fiber network." In: APL Photonics 7.1 (2022), p. 016106. DOI: 10.1063/5.0073040. eprint: https://doi.org/10.1063/5.0073040. URL: https://doi.org/10.1063/5.0073040.

[32] Krishnan R. Parameswaran, Jonathan R. Kurz, Rostislav V. Roussev, and Martin M. Fejer. "Observation of 99% pump depletion in single-pass second-harmonic generation in a periodically poled lithium niobate waveguide." In: Optics letters 27.1 (2002), pp. 43–45.

[33] Florian Kaiser, Bruno Fedrici, Alessandro Zavatta, Virginia d'Auria, and Sébastien Tanzilli. "A fully guided-wave squeezing experiment for fiber quantum networks." In: Optica 3.4 (2016), pp. 362–365.

[34] Samantha I. Davis, Andrew Mueller, Raju Valivarthi, Nikolai Lauk, Lautaro Narváez, Boris Korzh, Andrew D. Beyer, Olmo Cerri, Marco Colangelo, Karl K. Berggren, et al. "Improved heralded single-photon source with a photon-number-resolving superconducting nanowire detector." In: Physical Review Applied 18.6 (2022), p. 064007.

[35] Masahiro Takeoka, Rui-Bo Jin, and Masahide Sasaki. "Full analysis of multi-photon pair effects in spontaneous parametric down conversion based photonic quantum information processing." In: New Journal of Physics 17.4 (2015), p. 043030.

[36] Samantha I. Davis, Andrew Mueller, Raju Valivarthi, et al. "Improved Heralded Single-Photon Source with a Photon-Number-Resolving Superconducting Nanowire Detector." In: Phys. Rev. Appl. 18 (6 Dec. 2022), p. 064007. DOI: 10.1103/PhysRevApplied.18.064007. URL: https://link.aps.org/doi/10.1103/PhysRevApplied.18.064007.

[37] Enrico Pomarico, Bruno Sanguinetti, Nicolas Gisin, Robert Thew, Hugo Zbinden, Gerhard Schreiber, Abu Thomas, and Wolfgang Sohler. "Waveguide-based OPO source of entangled photon pairs." In: New Journal of Physics 11.11 (Nov. 2009), p. 113042. DOI: 10.1088/1367-2630/11/11/113042. URL: https://dx.doi.org/10.1088/1367-2630/11/11/113042.

[38] T. Brydges, A. S. Raja, A. Gelmini, et al. "Integrated photon-pair source with monolithic piezoelectric frequency tunability." In: Phys. Rev. A 107 (5 May 2023), p. 052602. DOI: 10.1103/PhysRevA.107.052602. URL: https://link.aps.org/doi/10.1103/PhysRevA.107.052602.

[39] Oliver Slattery, Lijun Ma, Kevin Zong, and Xiao Tang. "Background and review of cavity-enhanced spontaneous parametric down-conversion." In: Journal of Research of the National Institute of Standards and Technology 124 (2019), p. 1.

[40] Christopher L. Morrison, Francesco Graffitti, Peter Barrow, Alexander Pickston, Joseph Ho, and Alessandro Fedrizzi. "Frequency-bin entanglement from domain-engineered down-conversion." In: APL Photonics 7.6 (2022).

[41] CJ Xin, Jatadhari Mishra, Changchen Chen, Di Zhu, Amirhassan Shams-Ansari, Carsten Langrock, Neil Sinclair, Franco NC Wong, MM Fejer, and Marko Lončar. "Spectrally separable photon-pair generation in dispersion engineered thin-film lithium niobate." In: Optics Letters 47.11 (2022), pp. 2830–2833.

[42] Neil Sinclair, Erhan Saglamyurek, Hassan Mallahzadeh, et al. "Spectral multiplexing for scalable quantum photonics using an atomic frequency comb quantum memory and feed-forward control." en. In: Phys. Rev. Lett. 113.5 (Aug. 2014), p. 053603.

[43] Joseph M. Lukens and Pavel Lougovski. "Frequency-encoded photonic qubits for scalable quantum information processing." In: Optica 4.1 (2017), pp. 8–16.